# Computation of the band structure of two-dimensional Photonic Crystals with *hp* Finite Elements

K. Schmidt and P. Kauf

Research Report No. 2007-05
July 2007

Seminar für Angewandte Mathematik
Eidgenössische Technische Hochschule
CH-8092 Zürich
Switzerland

# Computation of the band structure of two-dimensional Photonic Crystals with *hp* Finite Elements

K. Schmidt and P. Kauf

Seminar für Angewandte Mathematik
Eidgenössische Technische Hochschule
CH-8092 Zürich
Switzerland

Research Report No. 2007-05 July 2007

**Abstract**

The band structure of 2D photonic crystals and their eigenmodes can be efficiently computed with the finite element method (FEM). For second order elliptic boundary value problems with piecewise analytic coefficients it is known that the solution converges extremly fast, i.e. exponentially, when using *p*-FEM for smooth and *hp*-FEM for polygonal interfaces and boundaries. In this article we discretise the variational eigenvalue problems for the transverse electric (TE) and transverse magnetic (TM) modes in scalar variables with quasi-periodic boundary conditions by means of *p*- and *hp*-FEM. Our computations show exponential convergence of the numerical eigenvalues for smooth and polygonal lines of discontinuity of dielectric material properties.

**Keywords and phrases:** *hp*-FEM, exponential convergence, corner singularities, photonic crystals, photonic band structure, quasi-periodic boundary condition

**Subject Classification:** 65N30, 78A45, 65Z05, 35B27

# 1 Introduction

Photonic crystals are refractive materials with a certain periodic structure in one, two or three directions [1]. The behaviour of light in such media strongly depends on its frequency. At so called "forbidden frequencies" lying in the *band gap* of a particular photonic crystal no wave propagation is possible [2]. Such effects allow for applications in photonics and optics. For manufacturing reasons photonic crystals with two-dimensional periodicity (see figure 1) are very attractive.

Many properties of electrons in semiconductors, which are well explained by quantum mechanics, translate to photonic crystals. Hence, models for the description of photonic crystals are similar to those in solid state physics. For the prediction of photonic crystal properties one relies on a model of an infinte crystal with perfect periodicity. By the Floquet-Bloch transformation [3] the Maxwell eigenvalue problem for the propagating frequencies in an infinite domain is reformulated into a set of eigenvalue problems in the *elementary cell*, parameterised by the quasi-momemtum $\mathbf{k}$. The relation between quasi-momentum and eigen frequencies is the well-known *band structure*.

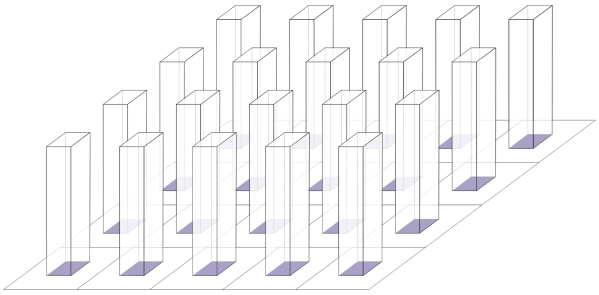

Figure 1: A photonic crystal with two-dimensional periodicity.

There is a wide variety of methods to calculate the band structure of photonic crystals [4]. One of the most popular methods is plane waves expansion (PWM) (see e.g. [5, 6, 1]), which is a fourier series in the quasi-momentum $\mathbf{k}$. A pure plane waves approach experiences convergence problems for high-contrast materials, an additional smoothing of the dielectric discontinuitites yields algebraic convergence in the number of expansion coefficients [7]. Other expansion based approaches are the method of Kohn, Korringa and Rostocker (KKR) [8, 9], the augmented plane waves expansion [10], which are both restricted to cylindrical structures, or the multiple multipole method (MMP) [11]. Separation of variable approaches are applied for crystals with quadratic veins [12, 13]. Furthermore, there are algorithms based on finite differences in time domain (FTDT) [14, 15, 16].

Unlike the previously mentioned methods, except FTDT, the finite element method [17] uses localised basis functions defined on a mesh. Since the mesh can be unstructured and even curved, the FE method is suitable for resolving complicated geometries. In its $h$-version, i.e. the mesh width $h$ is decreased, the numerical solutions of elliptic boundary value problems converge algebraically in the number of degrees of freedom ($N$). With $p$-FEM [18], where we enrich the trial space with higher order basis functions, *exponential convergence* in $N$ can be obtained, given that boundary and interfaces are smooth and the material coefficients are piecewise analytic. If, additionally, the boundary has corners, the solution is less regular, and a proper combination of mesh size $h$ refinement and element order $p$ enlargment, the $hp$-FEM [18], is needed to retain exponential convergence.

For transmission problems, where there are jumping material coefficients, one expects similar convergence behaviour, especially exponential convergence

- with $p$-FEM for smooth interfaces,
- with $hp$-FEM for polygonal interfaces, if the mesh is geometrically refined to the interface corners.

Nevertheless, to the knowledge of the authors, no paper discusses those adaptivity results for interface problems, especially not for band structure calculations of photonic crystals. However, we refer to the recent articles on $h$- and $p$-FEM for photonic crystals in 2D [19, 20] and 3D [21, 22].

The objective of this article is to study the convergence of Maxwell eigenvalues of two-dimensional photonic crystals with smooth or polygonal interfaces, respectively, with the above described refinement

strategies. We present an algorithm that computes the whole bandstructure quickly, because the entries of the system matrices are computed once and then changed only slightly for different $\mathbf{k}$ values.

In chapter 2 we formulate Maxwell's equations, which decouple into two scalar problems for the transverse electric (TE) and transverse magnetic (TM) fields. Then the periodicity in the dielectrical constant will allow us to use the Bloch transform to reformulate the eigenvalue problem on the infinite plane into a family of eigenvalue problems on the elementary cell with quasi-periodic boundary conditions. This family of problems is parametrised by the quasi-momentum $\mathbf{k}$. We establish weak formulations and discuss the regularity of the resulting eigenfunctions. This regularity is a criterion to choose between different strategies for designing the mesh and distributing the polynomial order to its cells.

In the following chapter 3 we describe the discretisation of the function spaces by *hp* finite elements on quadrilateral meshes with curved boundaries and with hanging nodes. First, the spaces with periodic boundaries are built. Then, we cut the basis functions into four parts, which are defined by the multiplication factors coming from the essential quasi-periodic boundary conditions. In the next step we assemble a system matrix for each pair of these parts. The sum of these totally sixteen matrices, each multiplied by the appropriate factor, gives us the overall system matrix for one specific $\mathbf{k}$ value.

We show numerical results in chapter 4. We compute the bandstructures of different geometries with curved and polygonal interfaces. A comparison to [12] and [13] validates the results produced by our algorithm. In a convergence analysis we confirm the following expectations:

- The convergence of *p*-FEM becomes worse if there are interface corners present.
- *p*-FEM converges only algebraically for geometries with interface corners, whereas *hp*-FEM recovers exponential convergence in the number of degrees of freedom.

We observe that the discretization error for *p*-FEM decreases faster than for *hp*-FEM up to a certain number of degrees of freedom. This effect is due to the relatively moderate singularities.

# 2 Problem formulation

## 2.1 Scalar equations for TE and TM mode

In three dimensional time-harmonic formulation Maxwell's equations for linear, non-magnetic media, without free charges or free currents, read

$$\operatorname{div}\mathbf{h}(\mathbf{x}) = 0, \qquad \mathbf{curl}\,\mathbf{e}(\mathbf{x}) = -\frac{i\omega}{c}\,\mathbf{h}(\mathbf{x}), \tag{1a}$$

$$\operatorname{div}(\varepsilon(\mathbf{x})\,\mathbf{e}(\mathbf{x})) = 0, \qquad \mathbf{curl}\,\mathbf{h}(\mathbf{x}) = \frac{i\omega}{c}\,\varepsilon(\mathbf{x})\,\mathbf{e}(\mathbf{x}), \tag{1b}$$

with $\mathbf{e}(\mathbf{x})$ and $\mathbf{h}(\mathbf{x})$ being the electric and magnetic field, respectivly, $\omega$ the angular frequency, $c$ the vacuum speed of light, $\varepsilon(\mathbf{x})$ the frequency-independent (relative) dielectrical constant. We assume lossless media, so $\varepsilon(\mathbf{x})$ is real. The dielectrical constant is bounded from below by 1 and from above by a positive constant $\varepsilon_{\max} < \infty$.

Together with the two constraint equations and a suitable decay condition for $|\mathbf{x}| \to \infty$, decoupling equations (1) leads to two equivalent eigenvalue problems

$$\mathbf{curl}\,\mathbf{curl}\,\mathbf{e}(\mathbf{x}) = \left(\frac{\omega}{c}\right)^2 \varepsilon(\mathbf{x})\,\mathbf{e}(\mathbf{x})\,, \tag{2a}$$

$$\mathbf{curl}\left(\frac{1}{\varepsilon(\mathbf{x})}\,\mathbf{curl}\,\mathbf{h}(\mathbf{x})\right) = \left(\frac{\omega}{c}\right)^2 \mathbf{h}(\mathbf{x})\,, \tag{2b}$$

i.e. they yield the same spectrum.
Since we consider $\varepsilon$ to be independent of the $x_3$-direction, we can split the electromagnetic fields in (2) into the transverse electric (TE) mode with $h^1 = h^2 = e^3 = 0$ and the transverse magnetic (TM) mode with $e^1 = e^2 = h^3 = 0$. Each mode yields a scalar and a vector valued problem. Because both, scalar and vector valued formulations, lead to the same spectrum, it is sufficient to consider the scalar problems for

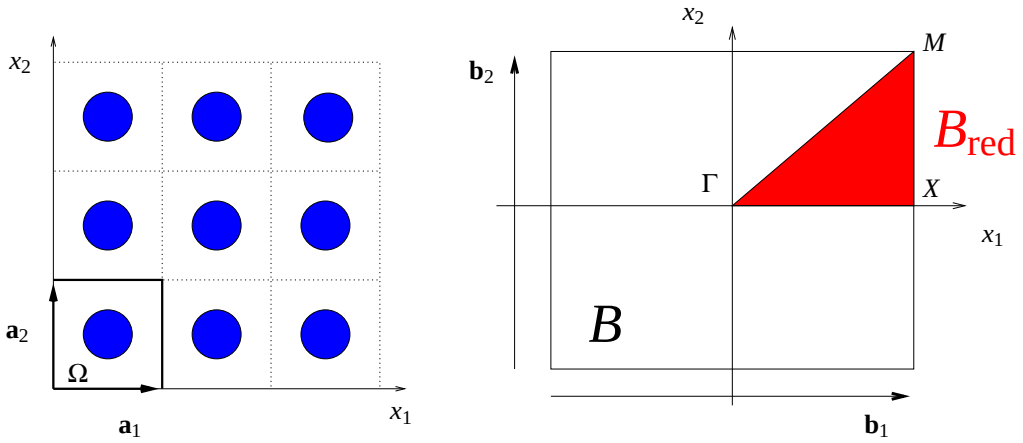


Figure 2: The left picture shows a two dimensional setting with periodicity domain $\Omega$. On the right side we see the corresponding Brillouin zone $B$ and the reduced Brillouin zone $B_{\text{red}}$ (red triangle).

TE and TM modes, which are Helmholtz like problems

$$-\operatorname{div}\mathbf{grad}\, e(\mathbf{x}) = \left(\frac{\omega}{c}\right)^2 \varepsilon(\mathbf{x}) e(\mathbf{x})\,, \tag{3-TM}$$

$$-\operatorname{div}\left(\frac{1}{\varepsilon(\mathbf{x})}\mathbf{grad}\, h(\mathbf{x})\right) = \left(\frac{\omega}{c}\right)^2 h(\mathbf{x})\,. \tag{3-TE}$$

The eigenfunctions of (3) fulfill the Neumann transmission condition

$$\left[\partial_{\mathbf{n}} e(\mathbf{x})\right] = \left[\frac{1}{\varepsilon(\mathbf{x})}\partial_{\mathbf{n}} h(\mathbf{x})\right] = 0, \tag{4}$$

where $[u]$ denotes the jump over an arbitrary piecewise smooth Lipschitz interface $\Gamma \subset \mathbb{R}^2$ with its unit normal vector $\mathbf{n}$, and $\partial_{\mathbf{n}} u(\mathbf{x}) := \mathbf{grad}\, u(\mathbf{x}) \cdot \mathbf{n}$.

## 2.2 The Bloch transformation onto the elementary cell

The photonic crystal is characterised by a periodic dielectrical constant

$$\varepsilon(\mathbf{x}+\mathbf{a}_i) = \varepsilon(\mathbf{x})\,,\ i = 1,2\,, \tag{5}$$

where the vectors $\mathbf{a}_i$ are the directions of periodicity. They span the fundamental periodicity domain $\Omega$ – a parallelogramm – which is also called *elementary cell*[1] (see Fig. 2). We regard $\Omega$ as a torus, i.e. opposite sides are identified with each other. We call the geometrical sides and corners of $\Omega$ $\Pi_i$ and $\Gamma_i$, respectively, with $i \in \{1,\dots,4\}$, the topological sides $\gamma_1$ and $\gamma_2$ and *the* topological corner $\pi$ (see Fig. 3).

The so called *reciprocal lattice* [23] with periodicity direction $\mathbf{b}_1$, $\mathbf{b}_2$ fulfilling

$$\mathbf{a}_i \cdot \mathbf{b}_j = 2\pi\delta_{ij}\,,\ i,j = 1,2 \tag{6}$$

is associated to the photonic crystal . The elementary cell of the reciprocal lattice is the Brillouin zone[2] $B$ – see Figure 2.

Now, let us define the Floquet-Bloch transform and its inverse [3] by

$$\widetilde{u}(\mathbf{k},\mathbf{x}) = (\mathscr{F}u)(\mathbf{k},\mathbf{x}) = \frac{1}{|B|} e^{-i\mathbf{k}\cdot\mathbf{x}} \sum_{\mathbf{m}\in\mathbb{Z}^2} u(\mathbf{x}-\mathbf{a}_\mathbf{m})\, e^{i\mathbf{k}\cdot\mathbf{a}_\mathbf{m}},$$

$$u(\mathbf{x}) = (\mathscr{F}^{-1}\widetilde{u})(\mathbf{x}) = \int_B \mathrm{e}^{i\mathbf{k}\mathbf{x}} \widetilde{u}(\mathbf{k},\mathbf{x})\, \mathrm{d}\mathbf{k},$$

[1] Note, that the elementary cell $\Omega$ is not uniquely defined by the vectors $\mathbf{a}_i$.

[2] The fundamental periodicity domain of the reciprocal lattice is not uniquely determined by $\mathbf{b}_1, \mathbf{b}_2$, so we impose the further condition that the Brillouin zone $B$ is the set of all points belonging to a fundamental periodicity domain of the reciprocal lattice, such that $\mathbf{k} \in B$ is closer to 0 than to any other point in the reciprocal lattice.

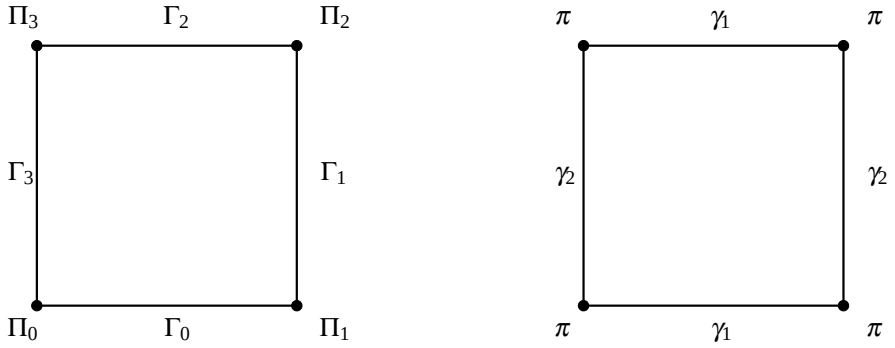


Figure 3: The geometrical sides and corners (left) and the topological ones (right) of the torus $\Omega$.

where $\mathbf{a_m} = m_1\,\mathbf{a}_1 + m_2\,\mathbf{a}_2$. The Floquet-Bloch transform has the same periodicity as the underlying pattern given by $\varepsilon(\mathbf{x})$, i.e. $\widetilde{u}(\mathbf{k},\mathbf{x}+\mathbf{a}_i) = \widetilde{u}(\mathbf{k},\mathbf{x})$, $i = 1,2$ for all $\mathbf{x} \in \mathbb{R}^2$.

The Floquet-Bloch transform is an isomorphism between $H^s(\mathbb{R}^2)$ and $H^s(\Omega \times B)$ ($s \in \mathbb{R}_+$) [3], and thus the problems (3) can be transformed onto $\Omega \times B$, with Neumann transmission condition (4) for the jump of $\tilde{e}(\mathbf{x})$ and $\tilde{h}(\mathbf{x})$ over opposite sides of $\Omega$ and modified differential operators. The whole spectrum of (2) is the union of the spectra for all $\mathbf{k} \in B$. We can regard $\mathbf{k} \in B$ as a parameter, and obtain a family of eigenvalue problems in $\Omega$.

However, we prefer the slightly different formulation for $e_\mathbf{k}(\mathbf{x}) := \mathrm{e}^{i\mathbf{kx}}(\mathscr{F}e)(\mathbf{x},\mathbf{k})$ and $h_\mathbf{k}(\mathbf{x}) := \mathrm{e}^{i\mathbf{kx}}(\mathscr{F}h)(\mathbf{x},\mathbf{k})$

$$-\operatorname{div}\mathbf{grad}\, e_\mathbf{k}(\mathbf{x}) = \left(\frac{\omega}{c}\right)^2 \varepsilon(\mathbf{x}) e_\mathbf{k}(\mathbf{x})\,, \tag{7-TM}$$

$$-\operatorname{div}\left(\frac{1}{\varepsilon(\mathbf{x})}\mathbf{grad}\, h_\mathbf{k}(\mathbf{x})\right) = \left(\frac{\omega}{c}\right)^2 h_\mathbf{k}(\mathbf{x})\,, \tag{7-TE}$$

with *quasi-periodic* boundary conditions

$$e_\mathbf{k}(\mathbf{x}+\mathbf{a}_i) = \mathrm{e}^{i\mathbf{ka}_i} e_\mathbf{k}(\mathbf{x})\,, \tag{8a}$$

$$h_\mathbf{k}(\mathbf{x}+\mathbf{a}_i) = \mathrm{e}^{i\mathbf{ka}_i} h_\mathbf{k}(\mathbf{x})\,, \tag{8b}$$

and the transmission conditions

$$\partial_\mathbf{n} e_\mathbf{k}(\mathbf{x}+\mathbf{a}_i) = \mathrm{e}^{i\mathbf{ka}_i} \partial_\mathbf{n} e_\mathbf{k}(\mathbf{x})\,, \tag{9a}$$

$$\frac{1}{\varepsilon(\mathbf{x}+\mathbf{a}_i)}\partial_\mathbf{n} h_\mathbf{k}(\mathbf{x}+\mathbf{a}_i) = -\mathrm{e}^{i\mathbf{ka}_i}\frac{1}{\varepsilon(\mathbf{x})}\partial_\mathbf{n} h_\mathbf{k}(\mathbf{x})\,, \tag{9b}$$

on $\partial\Omega$ ($i$ =1, 2), with $\mathbf{n}$ the outer normal vector on $\partial\Omega$.

Furthermore, if the pattern in the elementary cell has additional symmetry, e.g. mirror symmetry w.r.t. the diagonals, the so called reduced Brillouin zone $B_{\mathrm{red}} \subset B$ already contains the whole sprectrum (see Fig. 2). A widely used fact is, that in generic cases the band gaps are located at the boundary of $B_{\mathrm{red}}$, therefore the $\mathbf{k}$-values inside $B_{\mathrm{red}}$ can be neglected. In general however this is not true and we need the whole of $B_{\mathrm{red}}$ to determine the band gaps [23]. Also for the computation of other quantities such as the density of states or the Wannier functions the whole of $B_{\mathrm{red}}$ is needed.

## 2.3 Weak formulation

For the weak formulation of (7) we take the quasi-periodic boundary conditions (8) as essential and the transmission conditions (9) as natural boundary conditions. Thus, we define the function space

$$H^1_\mathbf{k}(\Omega) := \left\{ v \in H^1(\Omega) : v(\mathbf{x}+\mathbf{a}_i) = \mathrm{e}^{i\mathbf{ka}_i} v(\mathbf{x}) \text{ on } \partial\Omega,\, i = 1,2 \right\},$$

and obtain : For all $\mathbf{k} \in B_{\mathrm{red}}$ seek pairs $(h_\mathbf{k}, \omega_{\mathrm{TE}})$, $(e_\mathbf{k}, \omega_{\mathrm{TM}}) \in H^1_\mathbf{k}(\Omega) \times \mathbb{C}$, such that $\forall e'_\mathbf{k}, h'_\mathbf{k} \in H^1_\mathbf{k}(\Omega)$

$$\mathsf{a}_{\mathrm{TM}}(e_\mathbf{k}, e'_\mathbf{k}) = \left(\frac{\omega_{\mathrm{TM}}}{c}\right)^2 \mathsf{b}_{\mathrm{TM}}(e_\mathbf{k}, e'_\mathbf{k}), \tag{10-TE}$$

$$\mathsf{a}_{\mathrm{TE}}(h_\mathbf{k}, h'_\mathbf{k}) = \left(\frac{\omega_{\mathrm{TE}}}{c}\right)^2 \mathsf{b}_{\mathrm{TE}}(h_\mathbf{k}, h'_\mathbf{k}), \tag{10-TM}$$

with the inner products

$$\mathsf{a}_{\mathrm{TM}}(u,v) = \int_\Omega \mathbf{grad}\, u(\mathbf{x}) \cdot \overline{\mathbf{grad}\, v(\mathbf{x})}\, \mathrm{d}\Omega \;, \tag{11a}$$

$$\mathsf{b}_{\mathrm{TM}}(u,v) = \int_\Omega \varepsilon(\mathbf{x})\, u(\mathbf{x})\, \overline{v(\mathbf{x})}\, \mathrm{d}\Omega \;, \tag{11b}$$

$$\mathsf{a}_{\mathrm{TE}}(u,v) = \int_\Omega \frac{1}{\varepsilon(\mathbf{x})}\, \mathbf{grad}\, u(\mathbf{x}) \cdot \overline{\mathbf{grad}\, v(\mathbf{x})}\, \mathrm{d}\Omega \;, \tag{11c}$$

$$\mathsf{b}_{\mathrm{TE}}(u,v) = \int_\Omega u(\mathbf{x})\, \overline{v(\mathbf{x})}\, \mathrm{d}\Omega \;, \tag{11d}$$

where $\overline{v}$ is the complex conjugate of $v$.

The boundary terms from partial integration vanish due to the boundary conditions and cancellation of the factors $\mathrm{e}^{i\mathbf{k}\mathbf{a}_i}$ with their complex conjugates.

**Lemma 2.1.** *The eigenvalues $\omega_{TM}$ and $\omega_{TE}$ of* (10) *are real.*

*Proof.* Out of hermiticity in (11) it follows that all the eigenvalues $\left(\frac{\omega}{c}\right)^2 \in \mathbb{R}$. By choosing $e_{\mathbf{k}} = e'_{\mathbf{k}}$ and $h_{\mathbf{k}} = h'_{\mathbf{k}}$ in equation (10) we also get that $\left(\frac{\omega}{c}\right)^2 \geq 0$, implying $\omega \in \mathbb{R}$. □

**Lemma 2.2.** *Zero eigenvalues in* (10) *can only occur if $\boldsymbol{k} = 0$*

*Proof.* We introduce the space $H_{\mathbf{k},\infty} = H^1_{\mathbf{k}}(\Omega) \cap C^\infty(\Omega)$, which is dense in $H^1_{\mathbf{k}}(\Omega)$. If $\omega = 0$, then $a^{\mathbf{k}}_{\mathrm{TE}}(h_{\mathbf{k}}, h_{\mathbf{k}}) = 0$, which is the case only if $h_{\mathbf{k}} = \text{const}$. If $\mathbf{k} \neq 0$, the only constant function in $H_{\mathbf{k},\infty}$ is 0, but 0 is not an eigenfunction, which proves the lemma. □

## 2.4 Regularity of eigenfunctions

The regularity of the eigenfunctions $e_{\mathbf{k}}(\mathbf{x})$ or $h_{\mathbf{k}}(\mathbf{x})$ of (7) determines the accuracy of their representation in discrete trial spaces and determines which adaptive refinement strategy is optimal.

To analyze this regularity we look at the subdomains $\Omega_i \subset \Omega$, in which the dielectrical constant $\varepsilon(\mathbf{x})$ and also $\frac{1}{\varepsilon(\mathbf{x})}$ are analytic.

$$\varepsilon(\mathbf{x})\big|_{\Omega_i} \in \mathscr{A}(\Omega_i)$$

W.l.o.g. we assume that the elementary cell $\Omega$ is composed into two such domains $\Omega_1$ and $\Omega_2$, i.e.

$$\overline{\Omega} = \overline{\Omega_1} \cup \overline{\Omega_2}.$$

Their interface, assumed to be Lipschitz, is designated by $\Gamma := \partial\Omega_1 \cap \partial\Omega_2$. We consider a piecewise analytic interface $\Gamma$. There can be non-analytic points, i.e. there is no parametrisation around such points, for which arbitraryly high derivatives exist. We call these points *corners*, and the set of interface corners $\mathfrak{C}$.

### 2.4.1 Smooth interface

Let the interface be smooth, i.e. $\mathfrak{C} = \emptyset$. Then the eigenfunctions $e_{\mathbf{k}}(\mathbf{x})$ or $h_{\mathbf{k}}(\mathbf{x})$ of (7) are expected to be analytic in each subdomain up to the interface, i.e.

$$e_{\mathbf{k}}(\mathbf{x})\big|_{\overline{\Omega_i}} \in \mathscr{A}(\overline{\Omega_i}), \qquad h_{\mathbf{k}}(\mathbf{x})\big|_{\overline{\Omega_i}} \in \mathscr{A}(\overline{\Omega_i}), \qquad i = \{1,2\}.$$

Just on the interface $\Gamma$ there is a kink, but no singularity.

### 2.4.2 Polygonal interface

Now, let the interface contain corners. Then we can expect the eigenfunctions $e_{\mathbf{k}}(\mathbf{x})$ or $h_{\mathbf{k}}(\mathbf{x})$ to be analytic in each domain up to the interface corners $\mathfrak{C}$, i.e. for $i = \{1,2\}$

$$e_{\mathbf{k}}(\mathbf{x})\big|_{\overline{\Omega_i}\setminus\mathfrak{C}} \in \mathscr{A}(\overline{\Omega_i}\setminus\mathfrak{C}), \qquad h_{\mathbf{k}}(\mathbf{x})\big|_{\overline{\Omega_i}\setminus\mathfrak{C}} \in \mathscr{A}(\overline{\Omega_i}\setminus\mathfrak{C}).$$

At the material corners $\mathfrak{C}$ there is a singularity, i.e. there is a (higher order) derivative, which is not in $L^2(\Omega)$. The strengh of the singularity at a corner $\mathscr{C} \in \mathfrak{C}$ depends on the surrounding dielectrical constant and on the opening angle.

A technique to determine the singularity at $\mathscr{C}$ for the TE mode for straight material edges is to solve a local boundary value problem[3]

$$-\operatorname{div}\left(\frac{1}{\varepsilon(\mathbf{x})}\,\mathbf{grad}\, h_{\mathbf{k}}(\mathbf{x})\right) = 0$$

in polar coordinates in the neighbourhood of $\mathscr{C}$ (see e.g. [24]). This problem has a solution of the form $r^{\lambda}s(\phi)$. A more sophisticated technique to obtain the singularity functions, based on the Kondrat'ev method, is described in [25] for the 3D case. There, the techniques used for edge singularities are applicable for the point singularities in the 2D case.

### 2.5 Mesh design principles

For smooth interfaces the eigenfunctions are piecewise analytic. In the case where the interface is exactly resolved by element boundaries, it is well known [18], that *p*-FEM on a fixed mesh shows expontential convergence of eigenfunctions and eigenvalues in $N$

$$|\lambda - \lambda_N| \leq C\exp(-\beta N^{1/3}). \tag{12}$$

For polygonal interfaces the eigenfunctions are analytic up to the material corners and the singular functions are in the class of weighted spaces $\mathscr{B}^2_\beta(\Omega)$ [26, 27]. It is well known from *hp* theory [26, 27, 18], that in the case where the interface is exactly resolved by element boundaries and *hp* adaptive spaces are used, i.e. the mesh is refined towards the material corners $\mathfrak{C}$ and the polynomial degree is raised linearly away from $\mathfrak{C}$, the eigenfunctions are approximated with exponential convergence (12).

## 3 Algorithm

The finite elements are based on geometric meshes $\mathscr{M}$ on the periodic domain $\Omega$, whose construction is explained in section 3.1. In section 3.2 the basis functions, which span the periodic *hp*-adaptive finite element space on $\mathscr{M}$ are described. Each of these basis functions $b(\mathbf{x})$ is cut into the four parts $b^0(\mathbf{x}),...,b^3(\mathbf{x})$. Linear combinations of these parts with phase factors define an associated quasi-periodic basis function (Sec. 3.3). The system matrices of the discrete eigenvalue problem for each quasi-momentum $\mathbf{k}$ are constructed as a linear combination of phase factors and system matrices $\mathbf{A}^{mn}$, which are built out of combinations of the basis function parts $b^m(\mathbf{x})$ and $b^n(\mathbf{x})$ (Sec. 3.4).

### 3.1 Geometric meshes

The periodicity cell $\Omega$ is covered by a conforming quadrilateral mesh $\mathscr{M}_0$ with curvilinear quadrilateral cells, that resolves the material interfaces. Thus, material corners $\mathbb{C}$ are cell nodes and material interfaces $\mathbb{I}$ are represented by curved edges. Each cell is described by an element mapping $F_K$ from the reference cell $[0,1]^2$ (see Fig. 4).

As written in section 2.2, we regard $\Omega$ as a torus, i.e. opposite sides are identified with each other. To ensure this identification also for the mesh $\mathscr{M}_0$, opposite sides of $\Omega$ have the same subdivision into edges and opposite edges are topologically identical, as well as all the corners of $\Omega$ (see Fig. 3).

The *coarse mesh* $\mathscr{M}_0$ is the root of a family of meshes $\mathbb{M} = \{\mathscr{M}_i\}, i \in \mathbb{N}_0$. New entities, i.e. cells, edges and vertices, accrue in $\mathscr{M}_1$ by refining $\mathscr{M}_0$ geometrically towards the material corners. Thus, we subdivide those cells which touch a material corner $\mathscr{C} \in \mathbb{C}$ into four cells[4] (see figure 6). The mesh $\mathscr{M}_{i+1}$ is constructed by another subdivision of the smaller cells on $\mathbb{C}$ in $\mathscr{M}_i$. The meshes $\mathbb{M}$ that are constructed in the described way are called *geometric meshes* [18]. One could refine some cells around hanging nodes to obtain conforming meshes, however we decide to rather treat FE spaces with the up-coming non-conforming meshes than to introduce new cells (see mesh in Fig. 6).

[3] We expect the singularity to be the same for all $\mathbf{k}$.

[4] Our code is able to refine towards edges by subdivision of neighbouring cells into two cells [28]. Resolving material edges would be interesting as well, also with anisotropic polynomial degree. This however is beyond the scope of this article.

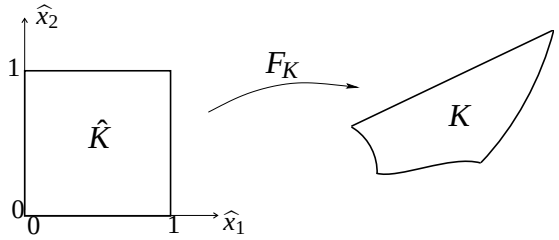


Figure 4: Element mapping from reference cell $\widehat{K}$ to physical cell $K$.

When we construct $\mathscr{M}_1$ by refining $\mathscr{M}_0$, we retain the set of cells and edges from $\mathscr{M}_0$ and store the newly created ones as children of their respective parent cells or parent edges (see Fig. 5). We use the same procedure to get $\mathscr{M}_{i+1}$ from $\mathscr{M}_i$. Thus, a cell or edge in $\mathscr{M}_i$ has at most $i$ ancestors. If cells and edges in $\mathscr{M}$ do not have any children, we say that they are on the lowest level.

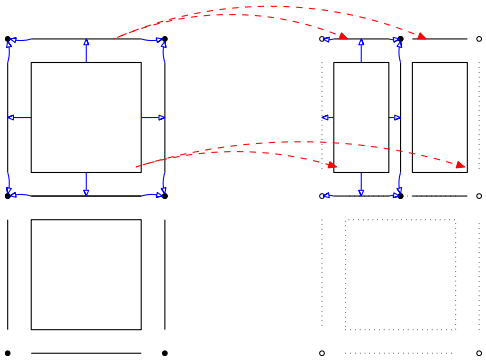

Figure 5: *Left* – topological entities in coarse mesh and their connections (solid arrows). *Right* – subdivided cells and edges are children of original one (dashed arrows).

This *parent-child-relationship* permits use to decide, whether an edge or a node is hanging or not. An edge is found to be hanging when itself as well as its ancestor are belonging to a lowest level cell. A node is hanging if it belongs to hanging edges only.

## 3.2 FE spaces with periodic boundary conditions

The FE space is based on elements, each consisting of a lowest level cell and shape functions, which are defined as tensor-products of polynomials on the reference element and then mapped to the cell.

For a particular adaptively refined mesh $\mathscr{M}$ we define a distribution of polynomial orders for the lowest level cells (Sec. 3.2.1). Together mesh and polynomial order distribution determine the basis functions, i.e. the identification of the basis functions with topological entities (Sec. 3.2.2), their support (Sec. 3.2.3) and their shape (Sec. 3.2.4). The shapes of the basis functions are defined on the so called support cells and then represented on the lowest level cells (Sec. 3.2.5).

### 3.2.1 Polynomial order in the cells

On each lowest level cell $c$ in the mesh $\mathscr{M}$ we determine the order[5] $p^c \in \mathbb{N}$, which will coincide with the maximal polynomial degree of the basis functions identified with that cell. These orders are collected in the vector $\mathbf{p}$. Thus, we obtain a mesh-degree combination $(\mathscr{M}, \mathbf{p})$, on which the periodic *hp*-FE spaces $\mathscr{S}_{\mathbf{0}}^{\mathbf{p},1}(\Omega, \mathscr{M}) \subset H_{\mathbf{0}}^1(\Omega)$ are based.

The basis functions of $\mathscr{S}_{\mathbf{0}}^{\mathbf{p},1}(\Omega, \mathscr{M})$ are periodic because the area $\Omega$ is regarded as a torus and the basis functions are continuous over all cell interfaces. For the quasi-periodic spaces $\mathscr{S}_{\mathbf{k}}^{\mathbf{p},1}(\Omega, \mathscr{M}) \subset$

[5] In fact we assign to each of these cell a pair of polynomial orders $\mathbf{p}_c \in \mathbb{N}^2$ for the two coordinates in the reference element. This functionality is here not needed, because we use here isotropic polynomial order in all cells.

$H^1_{\mathbf{k}}(\Omega)$ we adopt the concepts of continuity from $\mathscr{S}^{\mathbf{p},1}_{\mathbf{0}}(\Omega,\mathscr{M})$ and adapt the basis functions afterwards (see section 3.3), such that they fulfill (8).

Whereas our algorithm works with a general choice of polynomial orders $p_c$, we confine ourselves in this articles to orders that linearly increase away from the material corners [18, 28]. In the coarse mesh $\mathscr{M}_0$ all cells have got the same polynomial order. The linearly increasing polynomial orders appear since for the following meshes the polynomial order in the non-subdivided cells is raised by one (see figure 6).

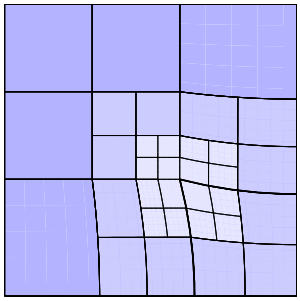

Figure 6: The mesh is refined towards the interface corners, while the polynomial order increases linearly away from material corners.

### 3.2.2 Identification of basis functions

The continuous basis functions of *hp*-adaptive FE spaces are classified by their identification with a topological entity, i.e. a node, an edge or a cell, of the mesh $\mathscr{M} \in \mathbb{M}$. Such a topological entity is called *active*, if it is identified with a basis function, i.e. it accomodates at least one degree of freedom.

The active cells are the cells on the lowest level. (At most) $(p^c-1)^2$ basis functions, the *internal basis functions*, are identified with them. Furthermore the non-hanging edges, which have no children or whose children are hanging, are active and $p_e-1$ basis functions are identified with them, where $p_e$ is the minimum of the polynomial orders of the adjacent cells. Finally there is exactly one related basis function for all non-hanging nodes.

### 3.2.3 Support of basis functions

Now, we want to determine the support of the basis functions, that we have just identified with a topological entity. More precicely that means we determine the cells, within which we are going to define the shape of the basis functions (see Sec. 3.2.4). We call these cells the *support cells* of a particular basis function. They have two properties :

- together they constitute the support of the basis function, and
- they are non-relative, i.e. none of them is the ancestor of another.

We denote by $c(e)$ and $c(v)$ the support cells of basis functions identified to an edge $e$ or vertex $v$, respectively. The support cell of an internal basis function is the cell $c$ itself.

For conforming meshes the surrounding cells of an edge $e$ or vertex $v$ on the lowest level constitute the support of the associated basis function. However, in non-conforming meshes the support cells $c(e)$ or $c(v)$ do not have to be on the lowest level.

The basis functions on an active edge $e$ have two support cells $c(e)$, one on each side of the edge[6]. Both of them have no child cell, which $e$ belongs to. However the support cells $c(e)$ could have children, if they were subdivided parallely to the edge $e$. This is illustrated in the left picture in figure 7.

Now, let us determine the support of the associated basis function for the node $v$. On each "side" of $v$ there can be several cells which $v$ belongs to. In each of these families[7] of cells we choose exactly one cell as support cell. Each of these support cells $c(v)$ have a non hanging common edge with two

[6] Due to the identification of two edges on $\partial\Omega$ there are no boundary edges.

[7] A family is a set of cells with parent child relationship.

adjacent support cells. In general these common edges however do not have to be active (see right picture in figure 7).[8]

In the next section we define the shape of the basis functions in the support cells and will represent it in each of the active cells[9] in section 3.2.5.

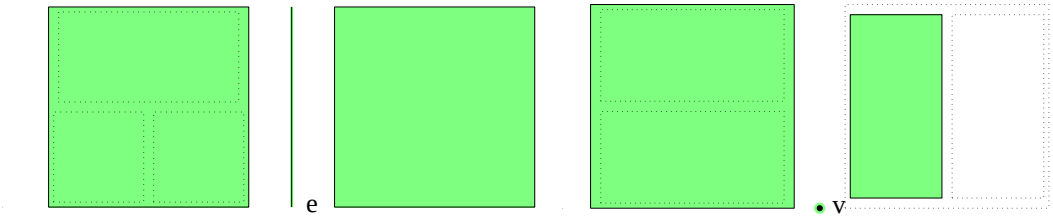


Figure 7: Support of basis functions on an edge $e$ (*left*) and on a vertex $v$ (*right*).

### 3.2.4 The shape of the basis functions

Now, we will construct the $i$-th periodic basis functions $\Phi_i(\mathbf{x})$ of the periodic space $\mathscr{S}_{\mathbf{0}}^{\mathbf{p},1}(\Omega,\mathscr{M})$. Their restriction $\Phi_i(\mathbf{x})|_K$ to a particular cell $K$ in their support is called local *shape function*. If $K$ is a support cell the local shape functions are defined as the "pushed back" reference element shape functions $\phi_{kl}(\widehat{\mathbf{x}})$ with $\widehat{\mathbf{x}} \in [0,1]^2$ and $k,l \in \mathbb{N}_0$, i.e.

$$\Phi_i(\mathbf{x})|_K = \pm\phi_{k,l}(F_K^{-1}\mathbf{x}), \tag{13}$$

The reference element shape functions are the tensor product

$$\phi_{k,l}(\widehat{\mathbf{x}}) = N_k(\widehat{x}_1)N_l(\widehat{x}_2)$$

of the hierarchical 1D basis [29]

$$N_k(\xi) = \begin{cases} 1-\xi & k=0 \\ \xi & k=1 \\ \xi(1-\xi)P_{k-2}^{1,1}(2\xi-1) & k>1 \end{cases}$$

with the Jacobi polynomials $P_{k-2}^{1,1}(\xi)$ [18], which are scaled integrated Legendre polynomials and can be computed by a recursion formula for any polynomial order.

If $\Phi_i(\mathbf{x})$ is identified with a node, then $k,l \leq 1$ in (13). For basis functions on an edge, there is either $k>1$ or $l>1$, for basis functions in the interior both indices are at least 2.

Let us consider the basis functions identified with an edge $e$, particularly their traces to $e$, which are polynomials. Whereas even polynomials do not change if the direction of the local variable $\xi$ along the edge switches, the odd polynomials change their sign. If the two neighbouring elements of $e$ have opposite directions of that local variable, on one side the shape function is multiplied by $(-1)$, i.e. there is a minus sign in (13).

When $K$ is in the support[10] of the basis function $\Phi_i(\mathbf{x})$, then it is represented by a linear combination of local shape functions, i.e.

$$\Phi_i(\mathbf{x})|_K = \sum_{k,l}[\mathbf{T}_K]_{kl,i}\phi_{kl}(F_K^{-1}\mathbf{x}), \tag{14}$$

where the shape functions $\phi_{kl}$ have a tensor product numbering. Note, that (13) is contained in (14).

The $\mathbf{T}$ matrices[11], also known as connectivity matrices, relate local to global shape functions and assure continuity of $\Phi_i(\mathbf{x})$, as well and especially on non-conforming meshes.

[8] Of course there could be several choices of the support cells. If the node already exists in the conforming mesh $\mathscr{M}_0$, then the neighbouring cells could be support cells in refined meshes as well. Since we are interested in small supports, we take the combination with smallest support cells.

[9] These are the cells on the lowest level.

[10] It has not to be the support cell.

[11] For conforming meshes the $\mathbf{T}$ matrices consist only of $+1$, $-1$ and zeros. If furthermore the maximal polynomial order is $p=2$ there are only ones and zeros.

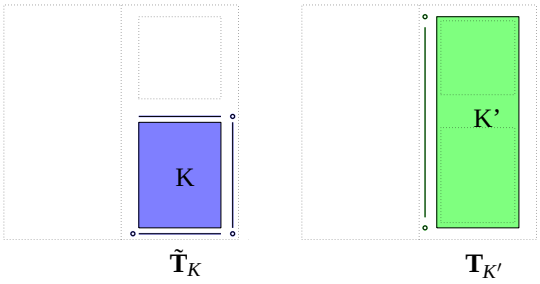


Figure 8: Basis functions for which $K$ is support cell (*left*) contribute to $\tilde{\mathbf{T}}_K$, whereas those for which the parent cell $K'$ is support cell (*right*) contribute to $\tilde{\mathbf{T}}_K$. The $\mathbf{T}$ matrix $\mathbf{T}_K$ results from (17).

#### 3.2.5 Representation on lowest level cells

Since the system matrices will be computed as integrals over the cells at the lowest level, the basis functions have to be represented on these cells, therefore the $\mathbf{T}$ matrices are needed there. The $i$-th column of the matrix $\mathbf{T}_K$ is the representation of the $i$-th basis function by all local shape functions of $K$, whenever $K$ lies fully in the support of the basis function. Otherwise the column contains only zeros. For a support cell $K$ we already defined the $i$-th column of the matrix $\mathbf{T}_K$ by (13), whereas for their successors we will do that in the following.

On each child $K'$ of the support cell $K$ the shape function is represented by shape functions in $K'$,

$$\phi_{kl}(F_{K'}^{-1}\mathbf{x})|_{K'} = \sum_{k',l'} [\mathbf{S}_{KK'}]_{k'l',kl}\, \phi_{k'l'}(F_{K'}^{-1}\mathbf{x}), \tag{15}$$

where the matrices $\mathbf{S}_{KK'}$ – the so called $\mathbf{S}$ matrices – are the tensor products of 1D $\mathbf{S}$ matrices [28].

Thus, with (15) and (14) the $i$-th $\mathbf{T}$ column of the child cell $K'$ follows as

$$[\mathbf{T}_{K'}]_i = [\mathbf{S}_{KK'}][\mathbf{T}_K]_i. \tag{16}$$

Some columns of the $\mathbf{T}$ matrix of the element $K'$ are received from the parent $K$ – where $K'$ is not support cell of the considered basis function –, whenever $K'$ is support cell the corresponding columns are assembled on $K'$ directly. Finally, the $\mathbf{T}$ matrix is defined by

$$\mathbf{T}_{K'} = \mathbf{S}_{KK'}\mathbf{T}_K + \tilde{\mathbf{T}}_{K'}, \tag{17}$$

where $\tilde{\mathbf{T}}_{K'}$ contains nonzero columns for basis functions for which $K'$ is support cell (see Fig. 8). These columns are defined by the support cell relation (13).

By applying (17) for the grandchildren of $K$ we compute their $\mathbf{T}$ matrices by repeatedly applying (17) for all the successors. Finally we can represent $\Phi_i(\mathbf{x})$ by shape functions on the cells at the lowest level.

### 3.3 FE spaces with quasi-periodic boundary conditions

Until now we have constructed the periodic *hp*-adaptives spaces $\mathscr{S}_{\mathbf{0}}^{\mathbf{p},1}(\Omega,\mathscr{M})$. The basis function, identified with the corner $\pi$ of $\Omega$ and these identified with a vertex or an edge on the sides $\gamma_1$ or $\gamma_2$, will be changed to fulfill the quasi-periodic boundary conditions (8). In other words, to each periodic basis function $b(\mathbf{x})$ we assign an appropiate quasi-periodic one $b^{\mathbf{k}}(\mathbf{x})$ for each $\mathbf{k}$. For basis functions in the interior of $\Omega$, where $b^{\mathbf{k}}|_{\partial\Omega} = 0$, quasi-periodic boundary conditions are trivially fulfilled, and they coincide for all $\mathbf{k}$ with the periodic counterpart.

In the following we derive the quasi-periodic functions $b^{\mathbf{k}}(\mathbf{x})$. For this we additionally have to distinguish between the geometrically different corners and sides. For notations we refer to Fig. 3.

First, we decompose the set of support cells $\mathbb{K}(b)$ for each basis function $b(\mathbf{x})$ in the periodic space

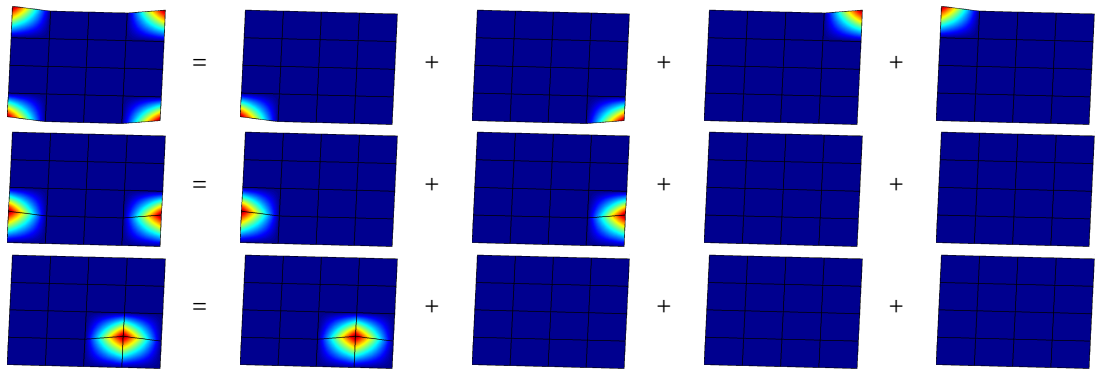

Figure 9: In the *top line* we see the basis function identified with the corner $\pi$ and its representation by functions belonging to one factor area. A basis function on the side $\gamma_2$ is shown in the *middle line*. These basis functions are cut into two parts, whereas basis functions in the interior $\Omega$ (*bottom line*) fully belong to one factor area.

$\mathscr{S}_{\mathbf{0}}^{\mathbf{p},1}(\Omega,\mathscr{M})$ into the four subsets[12]

$$\begin{aligned}
\mathbb{K}_3(b) &:= \{K \in \mathbb{K}(b) : b(\overline{K} \cap \Pi_2) > 0\},\\
\mathbb{K}_2(b) &:= \{K \in \mathbb{K}(b) : \exists \mathbf{x} \in \overline{K} \cap \Gamma_2 : b(\mathbf{x}) > 0\},\\
\mathbb{K}_1(b) &:= \{K \in \mathbb{K}(b) : \exists \mathbf{x} \in \overline{K} \cap \Gamma_1 : b(\mathbf{x}) > 0\},\\
\mathbb{K}_0(b) &:= \mathbb{K}(b) \setminus (\mathbb{K}_1(b) \cup \mathbb{K}_2(b) \cup \mathbb{K}_3(b)) \ ,
\end{aligned}$$

and $b(\mathbf{x})$ itself into the functions $b^0(\mathbf{x}),\ldots,b^3(\mathbf{x})$ (see Fig. 9) with

$$b^i(\mathbf{x}) := \begin{cases} b(\mathbf{x}) & \text{in } \mathbb{K}_i(b) \\ 0 & \text{otherwise.} \end{cases}$$

In Figure 9 this decomposition is shown. A basis function identified with the (topological) corner $\pi$ of $\Omega$ has got four support cells, each adjacent to a corner $\Pi_i$, and coincides with $\mathbb{K}_i(b)$. Thus, the four functions $b^i(\mathbf{x})$ represent the parts of $b(\mathbf{x})$ belonging to one of the four support cells, respectively. A basis function identified with a (topological) side, let it be $\gamma_1$, has support cells[13] on $\Gamma_1$ and $\Gamma_3$, $b^0(\mathbf{x})$ and $b^1(\mathbf{x})$ are the parts of $b(\mathbf{x})$ in these cells, respectively, the other functions $b^2(\mathbf{x})$ and $b^3(\mathbf{x})$ are zero. A basis function in the interior of $\Omega$ is cut into only one piece, namely $b^0(\mathbf{x})$. The other functions $b^1(\mathbf{x}),\ldots,b^3(\mathbf{x})$ are zero.

Now, the functions

$$b^{\mathbf{k}}(\mathbf{x}) := b^0(\mathbf{x}) + \mathrm{e}^{i\mathbf{k}\mathbf{a}_1} b^1(\mathbf{x}) + \mathrm{e}^{i\mathbf{k}\mathbf{a}_2} b^2(\mathbf{x}) + \mathrm{e}^{i\mathbf{k}(\mathbf{a}_1+\mathbf{a}_2)} b^3(\mathbf{x})$$

meet the quasi-periodicity conditions. The span of these functions defines the space $\mathscr{S}_{\mathbf{k}}^{\mathbf{p},1}(\Omega,\mathscr{M})$.

With the definition of the following factors

$$\phi_{\mathbf{k}}^0 := 1, \qquad \phi_{\mathbf{k}}^1 := \mathrm{e}^{i\mathbf{k}\mathbf{a}_1}, \qquad \phi_{\mathbf{k}}^2 := \mathrm{e}^{i\mathbf{k}\mathbf{a}_2}, \qquad \phi_{\mathbf{k}}^3 := \mathrm{e}^{i\mathbf{k}(\mathbf{a}_1+\mathbf{a}_2)},$$

we can write the quasi-periodic basis functions conveniently as

$$b^{\mathbf{k}}(\mathbf{x}) := \sum_n \phi_{\mathbf{k}}^n b^n(\mathbf{x}). \tag{18}$$

## 3.4 Assembly of the system matrices

For simplicity reasons we do not distinguish between TM and TE modes in this section. With the basis functions of the spaces $\mathscr{S}_{\mathbf{k}}^{\mathbf{p},1}(\Omega,\mathscr{M})$ defined just above, we find the matrix eigenvalue problems of (10)

$$\mathbf{A}^{\mathbf{k}}\vec{x}^{\mathbf{k}} = \lambda^{\mathbf{k}}\mathbf{M}^{\mathbf{k}}\vec{x}^{\mathbf{k}}$$

[12] This is possible if the mesh has at least two cells in each direction, which we "trivially" assume from now on.

[13] One on each side for basis functions identified with an edge, and two for those identified with a vertex.

with the system matrices

$$\mathbf{A}^{\mathbf{k}} = \left(\mathsf{a}(b_j^{\mathbf{k}}, b_j^{\mathbf{k}})\right)_{i,j=1}^{N}, \qquad \mathbf{M}^{\mathbf{k}} = \left(\mathsf{b}(b_j^{\mathbf{k}}, b_j^{\mathbf{k}})\right)_{i,j=1}^{N}, \tag{19}$$

where $\mathsf{a}$ and $\mathsf{b}$ stand for the appropiate inner product for the TM or TE mode, respectively. The eigenvalues are $\lambda^{\mathbf{k}} = \left(\frac{\omega}{c}\right)^2$. After inserting (18) into (19) we get

$$\mathbf{A}^{\mathbf{k}} = \sum_{m,n=0}^{3} \phi_{\mathbf{k}}^m \phi_{\mathbf{k}}^n \left(\mathsf{a}(b_j^m, b_j^n)\right)_{i,j=1}^{N},$$

and with the definition of the matrices

$$\mathbf{A}^{mn} := \left(\mathsf{a}(b_j^m, b_j^n)\right)_{i,j=1}^{N},$$

we write

$$\mathbf{A}^{\mathbf{k}} = \sum_{m,n=0}^{3} \phi_{\mathbf{k}}^m \phi_{\mathbf{k}}^n \mathbf{A}^{mn}.$$

Due to the cutting procedure, the computation of the sixteen matrices $\mathbf{A}^{mn}$ is exactly as expensive as the direct computation of $\mathbf{A}^{\mathbf{0}}$. The multiplication with the phase factors is neglegible compared to the overall cost. Thus, the assembly of an arbitrary number of the system matrices $\mathbf{A}^{\mathbf{k}}$ for different quasi-momenta $\mathbf{k} \in B_{\text{red}}$ has about the same cost as the assembly of the single matrix $\mathbf{A}^{\mathbf{0}}$. As basis functions in the interior of $\Omega$ are not affected by quasi-periodicity, only a small part of $\mathbf{A}^{\mathbf{k}}$ is affected when changing $\mathbf{k}$.

The integrals in (11) are computed by numerical Gauss quadrature on each element. The number of quadrature points is adapted to the maximal polynomial degree $p = p(c)$. We use sum factorisation [28] to reduce the integration costs from $O(p^6)$ to $O(p^5)$.

# 4 Numerical Results

The bandstructure algorithm is implemented in our object-oriented software package Concepts [30, 31], written in C++. The meshes use an exact representation of curved edges, which is needed for *p*-FEM and *hp*-FEM. In order to reduce the number of degrees of freedom, we use a truncated space[14]. For finding the smallest eigenvalues of the generalized matrix eigenvalue problems we use ARPACK [32], for the LU decomposition SuperLU [33].

## 4.1 Band structures and eigenfunctions

We calculated the band structure of four photonic crystals defined by the pattern of their elementary cells, the cylindrical holes, the dielectric veins (both in Fig. 10), the inversely curved dielectric cylinders and a $9 \times 9$ structure of dielectric veins with a periodic defect (both in Fig. 10).

In all cases the elementary cell is the square $\Omega = [0,a]^2$, which is scaled to $\widehat{\Omega} = [0,1]^2$, for which the Brillouin zone is $\widehat{B} = [0,2\pi]^2$. Then, the angular frequency $\omega$ scales with $1/a$. Hence, it is convenient to look at the non-dimensional quantity $\omega a/2\pi c = \sqrt{\widehat{\lambda}}/2\pi$, where $\widehat{\lambda}$ is the eigenvalue of the eigenvalue problem on $\widehat{\Omega}$.

The computed band structures of the four photonic crystals are shown in Figures 11 and 12. We want to emphasize that our algorithm is well suited for dielectric patterns with

- discontinuous dielectric constants,
- smooth, curved interfaces,
- straight and curved interfaces with corners,
- structures with small local geometry features.

[14] Only internal basis functions whose sum of the polynomial degree in the two coordinate directions is at most $p$, are included in the discrete space.

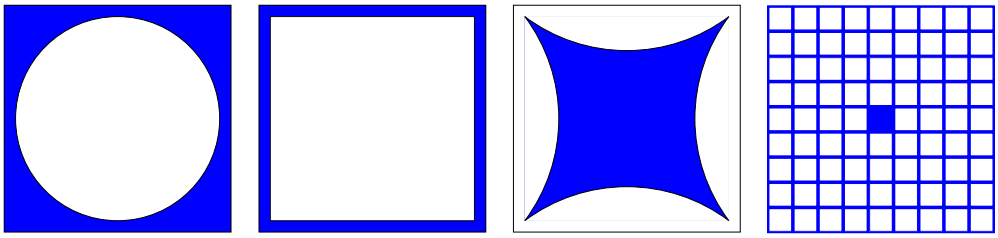

Figure 10: The elementary cell with cylindrical holes (*left*), that with dielectric veins (*inner left*), that with inversely curved dielectric rods (*inner right*) and that with a $9 \times 9$ structure of dielectric veins with a periodic defect in the middle (*right*). The white region is air ($\varepsilon = 1$), the blue region is a dielectric medium ($\varepsilon > 1$).

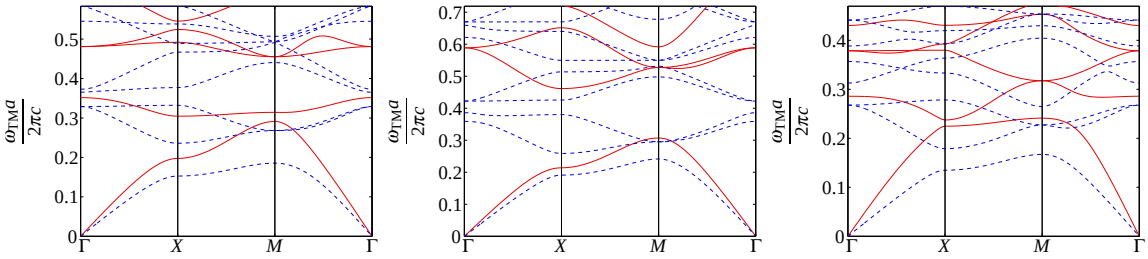


Figure 11: Bandstructure of the crystal with cylindrical holes of diameter $0.95\,a$ (*left*), of the crystal with dielectric veins of thickness $0.1\,a$ ($0.05\,a$ on both sides, *middle*) and of the crystal with inversely curved dielectric rods with radius $0.8\,a$ and distance between corners of $0.9\,a$. The dielectric medium has $\varepsilon = 20$. Solid lines denote TM modes, dashed lines denote the TE modes.

The refinement strategies will be discussed in section 4.2.

Although the band structure is shown for the symmetry lines of the reduced Brillouin zone only, the whole reduced Brillouin zone can be sampled conveniently, since the assembly of the matrices is done only once.

In addition to the eigenvalues the *hp*-adaptive FE algorithm also computes the eigenfunctions accurately. In Figure 12 we see the squared amplitude[15] of the TM and the TE mode of the first band at the *M* point for the crystal with the pertubated $9 \times 9$ dielectric vein structure (see Fig 10).

We have chosen the geometric and dielectric parameters for the crystal with dielectric veins (Fig. 10) the same as in [12, 13, 19]. In [12, 13] separation of variables approaches are applied, whereas in [19] first order FE are used. The comparison of these results to ours computed with *p*-FEM (see Tab. 1) validates our approach and our implementation. Notice the higher accuracy for the TM mode

[15] The squared amplitude corresponds to the concept of probability density in quantum electrodynamics.

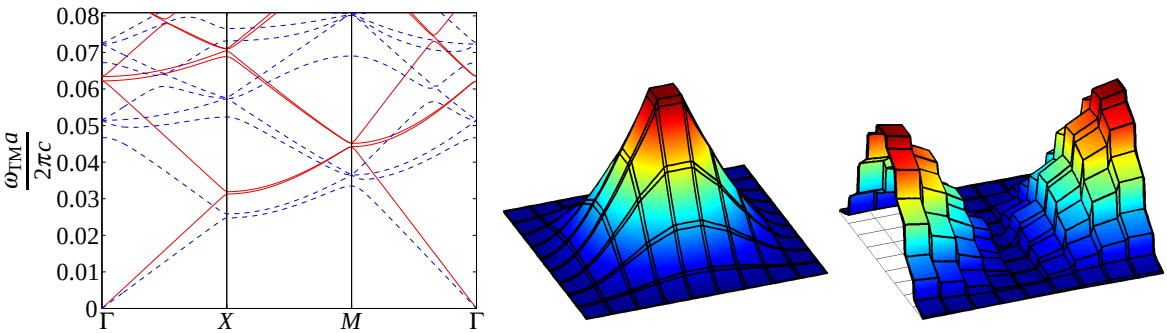


Figure 12: Bandstructure (*left*) of the crystal with a $9 \times 9$ structure of dielectric veins of thickness $0.1\,a/9$ and dielectric constant $\varepsilon = 20$, and the squared amplitude of the first TM eigenfunction $|e_{\mathbf{k}}(\mathbf{x})|^2$ (*middle*) and TE eigenfunction $|h_{\mathbf{k}}(\mathbf{x})|^2$ (*right*) at the *M* point. As the TE eigenvalue is twofold, there is another eigenfunction, which results from an interchange of $x_1$ and $x_2$.

for the same refinement level due to weaker singularities at the interface corners. We present further convergence results in section 4.2.

| | TM spectrum | | TE spectrum | | |
|---|---|---|---|---|---|
| Band No. | lower bound | upper bound | lower bound | upper bound | |
| 1 | 0 | 2.22 | 0 | 3.73 | from [12] |
| | 0 | 2.31 | 0 | 3.73 | from [13] |
| | 0 | 2.312 | 0 | 3.743 | from [19] |
| | 0 | 2.30429(73) | 0 | 3.719(34) | *p*-FEM |
| 2 | 2.64 | 5.09 | 8.42 | 13.73 | from [12] |
| | 2.64 | 5.09 | 8.43 | 13.76 | from [13] |
| | 2.650 | 5.099 | 8.440 | 13.704 | from [19] |
| | 2.642854(92) | 5.0873131(35) | 8.40(47) | 13.678(20) | *p*-FEM |
| 3 | 3.44 | 5.65 | 11.01 | 16.77 | from [12] |
| | 3.43 | 5.91 | 11.04 | 16.77 | from [13] |
| | 3.454 | 5.904 | 11.027 | 16.785 | from [19] |
| | 3.4379333(62) | 5.888(50) | 10.972(25) | 16.741(72) | *p*-FEM |

Table 1: The table shows our results for the relative eigenvalues $\widehat{\lambda} = \omega^2 a^2/c^2$ at the lower and upper bound of the first three bands for the dielectric veins (Fig. 10) in comparison to [12], [13], [19]. We use a polynomial refinement strategy with 9 cells and uniform polynomial order $p = 15$ (963 degrees of freedom). The results of [19] are converted with their given accuracy.

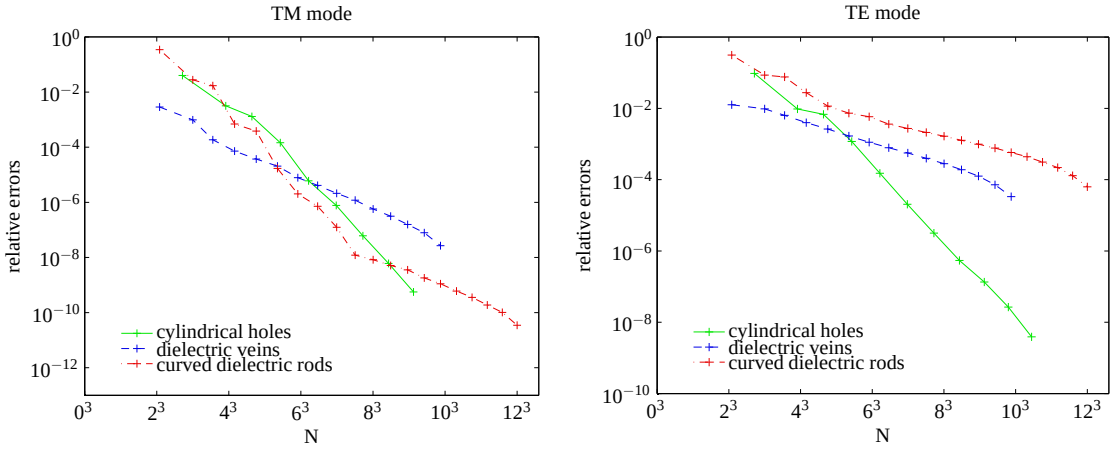


Figure 13: The convergence of the relative error for the smallest TM (*left*) and TE eigenvalue (*right*) at the midpoint of $\Gamma$ and $X$ for the crystals with cylindrical holes, with dielectric veins and with inversely curved rods (Fig. 10, same geometric and dielectric parameters as in Fig. 11). The computations were done with *p*-FEM.

## 4.2 Convergence of eigenvalues

Now, we investigate the convergence of the eigenvalues for different refinement strategies, starting with *p*-refinement. We choose the midpoint between $\Gamma$ and $X$, which is not a particular "good" one.

In Figure 13 the convergence of the smallest eigenvalue is shown for the crystals with cylindrical holes, with dielectric veins and with inversely curved rods (Fig. 10) – for the TM and the TE mode, computed with *p*-FEM. For the cylindrical holes with only smooth material interfaces we observe exponential convergence in the number of degrees of freedom $N$ as $\exp(-\beta N^{1/3})$ as we expected from

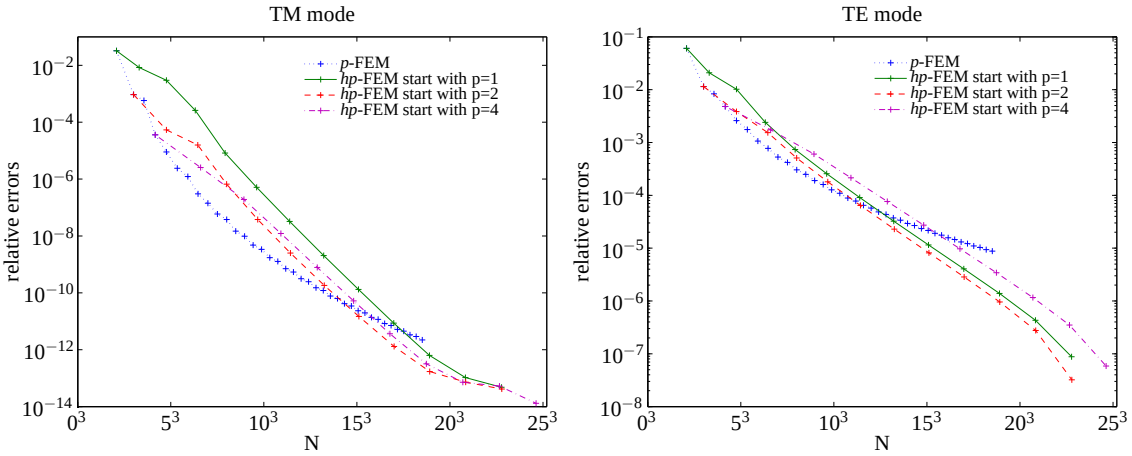


Figure 14: Convergence of the relative error for the TM-mode (*top*) and TE mode (*bottom*) of the crystal with dielectric veins ($\varepsilon = 8.9$, vein thickness 0.2 at each side). We use *p*-FEM and *hp*-FEM, the latter with different initial polynomial degree.

*hp*-theory [26, 27, 18]. For the crystals with dielectric veins and with inversely curved rods corner interfaces are present and the slope is less steep than for the crystal with cylindrical holes. Due to the smaller inward angle of the dielectric medium at the interface corners the singularity for the inversely curved rods is larger than for the dielectric veins [24], such that we observe a weaker convergence of the eigenvalues.

In Figure 13 the eigenvalues of the crystal with the dielectric veins and the inversely curved rods seem to converge exponentially for *p*-FEM, although interface corners are present. Nevertheless, if we continue with the $p$ refinement (in Fig. 14 for dielectric veins up to $p = 38$), merely algebraic convergence emerges[16].

In the following we investigate the convergence of the eigenvalues for geometric refinement – described in section 2.5 – in comparison to *p*-FEM. In Figure 14 the relative error of the smallest eigenvalue for the crystal with dielectric veins (Fig. 10) with thickness $0.4a$ and $\varepsilon = 8.9$ is shown. Starting with a coarse mesh with nine cells and $p = 1$ in all cells, *hp*-FEM shows exponential convergence in contrast to *p*-FEM, both for the TE and the TM mode. However, in the beginning the polynomial refinement performs better (up to $N \sim 4000$ for the TM mode, up to $N \sim 2000$ for the TE mode). Therefore we investigated the influence of the polynomial order in the coarse mesh for *hp*-FEM. The results in Figure 14 show, that an initial polynomial order of $p = 2$ performs better than one of order $p = 1$ for all $N$, and that $p = 4$ performs even better in the beginning, but converges with flatter slope. This behaviour is due to the weak singularities for the used material parameters. Note that the strategy reduces the relative error at about 8000 dof for the TM mode to the order of $10^{-14}$, but for the TE mode only to the order of $10^{-6}$.

Table 2 shows the numerical TE eigenvalues for the setting just described (as in the left diagramme in Fig. 14) for *hp*-FEM with initial polynomial order[17] $p = 2$, for *p*-FEM, and pure *h*-refinement ($p = 1$). *h*-FEM also converges algebraically, but more slowly than *p*-FEM. At *h*-FEM-level 6 ($N = 9216$) only three digits of the eigenvalue are exact, while with *p*-FEM at $N = 6345$ five digits are exact and with the described *hp*-FEM-strategy at $N = 6764$ (level 11) there are already six exact digits. With extrapolation of the *hp*-FEM-values we get 0.4914752, which we take for exact up to 7 digits (one more).

# 5 Conclusion

We introduced an algorithm based on *hp* finite elements with hanging nodes for computing the photonic crystal bandstructure. We showed that the eigenvalues converge exponentially for smooth and polygonal interfaces. In examples with polygonal interfaces we observed faster convergence with pure polynomial enrichment (*p*-FEM) for the first refinement levels than with *hp*-FEM – both for the TM and the TE

[16] With large convergence rate.

[17] More exactly, geometric refinement starts after a first *p*-refinement step.

| | *h*-FEM | | *p*-FEM | | *hp*-FEM | |
|---|---|---|---|---|---|---|
| level | #dof | $\frac{\omega_{\mathrm{TE},0}a}{2\pi c}$ | #dof | $\frac{\omega_{\mathrm{TE},0}a}{2\pi c}$ | #dof | $\frac{\omega_{\mathrm{TE},0}a}{2\pi c}$ |
| 1 | 9 | **0**.521302619112 | 9 | **0**.521302619112 | 9 | **0**.521302619112 |
| 2 | 36 | **0**.501735291198 | 27 | **0.49**7095810781 | 27 | **0.49**7095810781 |
| 3 | 144 | **0.49**4952283861 | 45 | **0.49**5570239622 | 108 | **0.49**3365508380 |
| 4 | 576 | **0.49**2664756896 | 72 | **0.49**3837964737 | 268 | **0.49**2231220419 |
| 5 | 2304 | **0.491**885702189 | 108 | **0.49**2751880410 | 512 | **0.491**725406461 |
| 6 | 9216 | **0.491**618020101 | 153 | **0.49**2340949399 | 904 | **0.491**563775139 |
| 7 | | | 207 | **0.491**998065356 | 1492 | **0.491**506786403 |
| 8 | | | 270 | **0.491**855851430 | 2324 | **0.4914**86485296 |
| 9 | | | 342 | **0.491**735848233 | 3448 | **0.49147**9231178 |
| 10 | | | 423 | **0.491**681227299 | 4912 | **0.49147**6634000 |
| 11 | | | 513 | **0.491**624540578 | 6764 | **0.491475**702552 |
| 12 | | | 612 | **0.491**597555930 | 9052 | **0.491475**368251 |
| 13 | | | 720 | **0.491**568698587 | 11824 | **0.491475248**235 |
| 14 | | | 837 | **0.491**554083965 | | |
| 15 | | | 963 | **0.491**537578751 | | |
| 18 | | | 1395 | **0.491**513511149 | | |
| 23 | | | 2295 | **0.4914**93587640 | | |
| 28 | | | 3420 | **0.4914**85836966 | | |
| 33 | | | 4770 | **0.4914**81669113 | | |
| 38 | | | 6345 | **0.49147**9554612 | | |

Table 2: Convergence of the first eigenvalue for the TE mode for the crystal with dielectric veins (see Fig. 10, $\varepsilon = 8.9$, vein thickness 0.2 at each side) at $\mathbf{k} = (1/2a, 0)$ for pure mesh refinement (*h*-FEM), pure polynomial order enlargment (*p*-FEM) and adaptive *hp*-FEM. For *p*-FEM and *hp*-FEM the level corresponds to the maximal polynomial degree in the discrete space. With *hp*-FEM we first refine only the polynomial degree and start then with geometric mesh refinement towards the four interface corners. With extrapolation (exponential ansatz) we expect $\omega_{\mathrm{TE},0}a/2\pi c \approx 0.4914752$.

mode. This is due to the relatively weak singularities. The discretisation error of pure cell refinement (*h*-FEM) shows much slower convergence. These results meet the expectations from the *hp*-FEM theory.

The presented algorithm is able to compute the bandstructure for polygonal shaped elementary cells to a high accuracy at low computational costs. This is due to the exponential convergence of *hp*-FEM and because the system matrices are assembled only once for the whole Brillouin zone.

In further research possible improvements of the eigenvalue solver could be investigated, e.g. the reuse of eigenvectors as start vectors at slightly different $\mathbf{k}$ points.

# 6 Acknowledgement

The authors would like to thank Prof. R. Hiptmair, Prof. Ch. Schwab (both ETH Zürich, Switzerland) and Prof. M. Dauge (Université de Rennes 1, France) for their support and assistance.

# References

[1] J. D. Joannopoulos, R. D. Meade, and J. N. Winn. *Photonic Crystals: Molding the Flow of Light*. 1995.

[2] Eli Yablonovitch. Inhibited spontaneous emission in solid-state physics and electronics. *Phys. Rev. Lett.*, 58(20):2059–2062, May 1987.

[3] Peter Kuchment. *Floquet Theory for Partial Differential Equations*. Birkhäuser Verlag, Basel, 1993.

[4] K. Busch. Photonic band structure theory: assessment and perspectives. *Compte Rendus Physique 3, 53-66*, 3(53):53–66, 2002.

[5] Robert D. Meade, Karl D. Brommer, Andrew M. Rappe, and J. D. Joannopoulos. Existence of a photonic band gap in two dimensions. *Appl. Phys. Lett.*, 61(4):495–497, Jul 1992.

[6] R.D. Meade, A.M. Rappe, K.D. Brommer, J.D. Joannopoulos, and O.L. Alerhand. Accurate theoretical-analysis of photonic band-gap materials. *Physical Review B*, 48(11):8434–8437, Sep 1993.

[7] Steven G. Johnson and J. D. Joannopoulos. Block-iterative frequency-domain methods for maxwell's equations in a planewave basis. *Optics Express*, 8(3):173–190, Jan 2001.

[8] K. M. Leung and Y. Qiu. Multiple-scattering calculation of the two-dimensional photonic band structure. *Phys. Rev. B*, 48(11):7767–7771, Sep 1993.

[9] Kazuo Ohtaka, Tsuyoshi Ueta, and Katsuki Amemiya. Calculation of photonic bands using vector cylindrical waves and reflectivity of light for an array of dielectric rods. *Phys. Rev. B*, 57(4):2550–2568, Jan 1998.

[10] W. C. Sailor, F. M. Mueller, and Pierre R. Villeneuve. Augmented-plane-wave method for photonic band-gap materials. *Phys. Rev. B*, 57(15):8819–8822, Apr 1998.

[11] Esteban Moreno, Daniel Erni, and Christian Hafner. Band structure computations of metallic photonic crystals with the multiple multipole method. *Phys. Rev. B*, 65(15):155120, Apr 2002.

[12] Alexander Figotin and Yuri A. Godin. The computation of spectra of some 2D photonic crystals. *Journal of computational physics*, 136:585–598, 1997.

[13] Igor Ponomarev. Separation of variables in the computation of spectra in 2-D photonic crystals. *SIAM Journal on Applied Mathematics*, 61(4):1202–1218, 2001.

[14] J. B. Pendry and A. MacKinnon. Calculation of photon dispersion relations. *Phys. Rev. Lett.*, 69(19):2772–2775, Nov 1992.

[15] C. T. Chan, Q. L. Yu, and K. M. Ho. Order-n spectral method for electromagnetic waves. *Phys. Rev. B*, 51(23):16635–16642, Jun 1995.

[16] Kazuaki Sakoda and Jun Kawamata. Novel approach to photonic bands with frequency-dependent dielectric constants. *Optics Express*, 3(1):12–18, July 1998.

[17] Dietrich Braess. *Finite Elemente*. Springer, Berlin, 2003.

[18] Christoph Schwab. *p- and hp- Finite Element Methods: Theory and Applications in Solid and Fluid Mechanics*. Oxford University Press, 1998.

[19] Waldemar Axmann and Peter Kuchment. An efficient finite element method for computing spectra of photonic and acoustic band-gap materials i. scalar case. *Journal of Computational Physics*, 150:468–481, 1999.

[20] David C. Dobson. An Efficient Method for Band Structure Calculations in 2D Photonic Crystals. *Journal of Computational Physics*, 149(2):363–376, March 1999.

[21] David C. Dobson, Jayadeep Gopalakrishnan, and Joseph E. Pasciak. An efficient method for band structure calculations in 3d photonic crystals. *Journal of Computational Physics*, 161(2):668–679, July 200.

[22] Daniele Boffi, Matteo Conforti, and Lucia Gastaldi. Modified edge finite elements for photonic crystals. *Numerische Mathematik*, 105(2):249–266, Dec 2006.

[23] Charles Kittel. *Introduction to Solid State Physics*. John Wiley and Sons, New York, 2004.

[24] Martin Petzold. *Regularity and error estimates for elliptic problems with discontinuous coefficients*. PhD thesis, FU Berlin, Berlin, Jan 2001.

[25] M. Costabel, M. Dauge, and S. Nicaise. Singularities of Maxwell interface problems. *Rairo-mathematical Modelling Numerical Analysis-modelisation Mathematique Et Analyse Numerique*, 33(3):627–649, 1999.

[26] I. Babuška, B. Q. Guo, and J. E. Osborn. Regularity and numerical solution of eigenvalue problems with piecewise analytic data. *SIAM J. Numer. Anal.*, 26(6):1534–1560, 1989.

[27] Ben Qi Guo and Hae Soo Oh. The *h-p* version of the finite element method for problems with interfaces. *Internat. J. Numer. Methods Engrg.*, 37(10):1741–1762, 1994.

[28] Philipp Frauenfelder. *hp-Finite Element Methods on Anisotropically, Locally Refined Meshes in Three Dimensions with Stochastic Data*. PhD thesis, ETH Zürich, Zürich, 2004.

[29] George Em Karniadakis and Spencer J. Sherwin. *Spectral/hp Element Methods for Computational Fluid Dynamics*. Oxford University Press, Oxford, 1999.

[30] Philipp Frauenfelder and Christian Lage. Concepts – An Object-Oriented Software Package for Partial Differential Equations. *Mathematical Modelling and Numerical Analysis*, 36(5):937–951, September 2002.

[31] Concepts Development Team. Concepts homepage. http://www.concepts.math.ethz.ch, 2003.

[32] R.B. Lehoucq, D.C. Sorensen, P.A. Vu, and C. Yang. Arpack: Fortran subroutines for solving large scale eigenvalue problems.

[33] James W. Demmel, Stanley C. Eisenstat, John R. Gilbert, Xiaoye S. Li, and Joseph W. H. Liu. A supernodal approach to sparse partial pivoting. *SIAM J. Matrix Analysis and Applications*, 20(3):720–755, 1999.